Thermodiffusion in magnetic colloids evidenced and studied by forced Rayleigh scattering experiments

J. Lenglet, A. Bourdon, J. C. Bacri, and G. Demouchy
Laboratoire des Milieux Désordonnés et Hétérogènes CNRS, UMR 7603, Université Pierre et Marie Curie, Case 86, 4 place Jussieu, 75252 Paris Cedex 05, France
(Received 27 June 2001; published 5 March 2002)

This paper shows how forced Rayleigh scattering can be used as an experimental tool for studying thermodiffusion (Soret effect). The systems investigated are magnetic colloids of different types. A framework including thermodiffusion and dielectrophoresis is described in which the evolutions of temperature and of colloid concentration are clearly distinguished. The framework is then shown to account for experiments on steady-state concentration gratings coupled with transient temperature ones, and the parameters are determined therefrom. Dielectrophoretic forces are found to be negligible. Studying different types of magnetic colloids with various dilution rates shows that the sign of the Soret effect is controlled by the nature of the particle coating made up of electrostatic charges or of surfactant, and that its mechanism is located at the nanoparticle core-solvent interface.

DOI: 10.1103/PhysRevE.65.031408 PACS number(s): 82.70.Dd, 42.65.Es, 75.50.Mm, 66.90.+r

I. INTRODUCTION

Forced Rayleigh scattering (FRS) is a powerful technique for studying heat and mass transfers [1–4] and has been used by us with magnetic colloids recently [5]. These colloids, also called ferrofluids, are divided in two classes, ionic or surfacted, according to the nature of the interparticle repulsion: electrostatic if the particles are coated with ionic ligands, steric if the particles are coated with surfactants [6,7]. Ferrofluids exhibit very interesting properties under an applied magnetic field [8–14] and have many technical uses [15–17].

If a magnetic colloid sample is placed in the interference region of two coherent intersecting laser beams (called here pump beams) having the same polarization directions, the nanoparticle concentration and, therefore, the index of refraction become spatially modulated with the same periodicity as that of the interference pattern [5]. The sample works as a diffracting grating that is probed by a cw laser beam. If the interfering beams are switched off, the grating vanishes because the colloid concentration becomes homogeneous again through diffusion processes. The decay of the diffracted probe-beam intensity provides information about them because it follows an exponential law with a rate proportional to the nanoparticle diffusion coefficient D_m. As diffusion processes are slow ($D_m \approx 10^{-11}$ m^2 s^{-1}) [5], conventional tracer techniques are time consuming. In a FRS experiment, this problem is bypassed as diffusion processes take place on very short lengths ranging from 20 to 65 μm, leading to decay times of some seconds, allowing extensive measurements.

However, the concentration gratings we observed in our samples exhibited such a strong contrast that their buildup mechanism was not clear up to now [5]. To find it, two possible mechanisms seem to be worth exploring. In the first one, the force acting on nanoparticles has a dielectric origin: the particles and the solvent are differently polarized by the electric fields of the pump beams, which yields a force proportional to the gradient of light intensity. This force is termed here dielectrophoretic by analogy with the electrophoretic force. In the second possibility, the observed mass flow is due to thermodiffusive effect [18,19], also called Soret effect [20], in which the mass flow is induced by a gradient of temperature. This explanation based on a thermal effect is consistent with our previous qualitative observations that large FRS signals are only found in optically absorbing samples [5,8]. After briefly recalling our colloidal system and the FRS setup in Sec. II, a model is presented in Sec. III and Sec. IV in which both dielectrophoretic and thermodiffusive effects are taken into account simultaneously, and in which temperature and nanoparticle-concentration variations are determined at the same time. The question whether the diffracted intensity is mainly due to an index or to an absorption grating is also answered by complementary optical measurements (Appendix and Sec. V). Our model and related experimental procedure are first validated by experiments carried out on the magnetic colloid sample that provides the largest and clearest signals (Sec. V). Experimental diffraction results obtained under various geometrical conditions and with different types of colloids, ionic or surfacted, will lead us to a deeper analysis of the origin of the Soret effect in these colloids (Secs. VI and VII).

II. MAGNETIC COLLOIDS AND FRS EXPERIMENTAL SETUP

Our magnetic liquids (or ferrofluids) are colloidal solutions of nanosized magnetic oxide particles dispersed in a liquid carrier that are chemically synthesized after Massart's method [21]. In this work, particle cores are made of either maghemite (γ-Fe_2O_3) or cobalt ferrite ($CoFe_2O_4$); they are magnetic monodomains bearing a magnetic moment of about 10^4 μ_B. van der Waals and magnetic-dipolar interactions between particles are of the same order of magnitude as k_BT, k_B being the Boltzmann constant. Thus the colloidal stability of these dipolar solutions has to be ensured by an additional interparticle repulsion: electrostatic in a polar carrier (in this

TABLE I. Structure and mass-diffusion properties of the magnetic colloids under study. The structure of the studied magnetic colloids is as follows. The particle core is made up of maghemite (γ-Fe_2O_3) or cobalt ferrite ($CoFe_2O_4$), and is denoted ''207'' or ''184,'' respectively. In surfacted samples, the solvent is cyclohexane (C_6H_{12}) or toluene (C_7H_8) and is denoted ''CX'' or ''Tol,'' respectively; the surfactant is denoted ''BNE'' or ''OA'' for Beycostatne or oleic acid, respectively. In ionic samples, nanoparticles are dispersed in water, colloids are stabilized by citrate (''Cit'') or H^+ ligands, with Na^+ (pH$\approx$7) or NO_3^- (pH$\approx$2) counterions, respectively. Nanoparticle-diffusion coefficients D_m are mainly measured according to the method given in Ref. [5] or in Sec. VII, which gives the hydrodynamic radius R_H through the Stokes-Einstein equation ($6\pi D_m R_H \eta = k_B T$). Solvent viscosity η is found in Ref. [25]. Estimated D_m values are calculated from an already known value of R_H. The mean radius R_{RX} of the nanoparticle core, is determined by x-ray diffraction measurements with a good accuracy, which is not in contradiction with the observed large polydispersity [24,32]. Symbol $\approx$ before a number indicates a value estimated from nearby data.

Sample name		Structure		$10^{12} D_m$ ($m^2\,s^{-1}$)	$10^3\,\eta$ (Pa s)	R_H (nm)	R_{RX} (nm)
Surfacted	Surfactant	Core	Solvent				
CX207BNE	Beycostatne	γ-Fe_2O_3	C_6H_{12}	30.6±5	0.98	7.16±1.2	4.82
Tol207BNE	Beycostatne	γ-Fe_2O_3	C_7H_8	≈51	0.59	≈7.16	4.82
CX207OA	Oleic acid	γ-Fe_2O_3	C_6H_{12}	≈30.6	0.98	≈7.16	4.82
Ionic	Stabilization	Core	Counter-ion				
V207NO3	H^+	γ-Fe_2O_3	NO_3^-	36±5	1.002	5.95±0.8	4.82
V207Cit	Citrate	γ-Fe_2O_3	Na^+	21±6	1.002	10.2±3	4.82
S184	Citrate	$CoFe_2O_4$	Na^+	≈17.3	1.002	≈12.4	7.05

work, water), and steric in a nonpolar one. In aqueous media, nanoparticles are macroions coated with surface ligands that give a surface-charge density $\sigma(|\sigma| \approx 2\times10^{-3}\ \mathrm{C\,m^{-2}})$. Ligands are either hydroxo ones at pH$\approx$2 ($\sigma>0$ with NO_3^- counterions) or citrate ones at pH$\approx$7 ($\sigma<0$ with Na^+ counterions). In nonpolar media, a surfactant coating is added to the particles to provide interparticle steric hindrance. The colloidal stability of most of the samples has been checked under a 1 T magnetic field by a diffraction method [7]. The characteristics of all the studied samples are given in Table I. A large part of the paper is devoted to the presentation of a method for proving and measuring the Soret effect in a ferrofluid; this method is often tested experimentally with the most efficient sample we have. It is based on maghemite particles coated with Beycostatne® surfactant (also called BNE) and dispersed in cyclohexane. This ferrofluid is called ''CX2O7BNE'' in this paper, whatever its dilution rate.

In the FRS technique, a transient grating generated in the sample by the interference pattern of two coherent pump beams diffracts a probe laser beam (Fig. 1). This grating is due to space-periodic variations of the volume fraction Φ in nanoparticles, and of temperature T in the sample. The Q-switched mode-locked Nd:YAG (yttrium aluminum garnet) pump laser used in the experiments provides 80-ps-wide pulses that are gathered, with a variable repetition rate, in 150-ns-long trains. A 25-pulse train is short enough to be considered as a Dirac function in our further analysis. The pump-laser beam is frequency doubled ($\lambda_p = 532$ nm) so as to be strongly absorbed in the ferrofluid, and the residual infrared light is separated out by means of a prism. The second-harmonic green light beam is split into two beams that interfere inside the sample with a well-defined angle θ by means of a 50/50% beam splitter, which provides a good contrast to the pump interference pattern of 400 μm diameter (Fig. 1). A direct optical observation setup helps to make sure that the interference pattern is really located within the thin sample cell (10 to 400 μm thick); this setup is also used to determine the incident beam diameter by counting the pattern interfringes. A He-Ne cw probe laser beam (350 to 400 μm diameter) is sent onto an area of the sample that includes the interference zone so as to obtain a first-order diffracted beam whose intensity is analyzed. For a reliable numerical analysis, the detection setup (optical attenuators, wavelength selecting filters, photomultipliers, digitizer, averager, etc.) is carefully chosen so as to bring no distortion to the signal.

III. TWO-TIME-SCALE MODEL

The coupled variations of the four following quantities, the particle volume-fraction Φ, the volume-fraction flow density $\mathbf{J}_m$, the temperature T, and the heat flow density $\mathbf{J}_{\mathrm{th}}$ in the sample, will now be studied according to the conventional theory of transport phenomena. In the absence of convection they obey the following equations:

$$\mathbf{J}_m = -D_m[\boldsymbol{\nabla}\Phi + S_T \boldsymbol{\nabla} T + (\Phi/k_B T)\boldsymbol{\nabla} U_d], \tag{3.1}$$

and

$$\mathbf{J}_{\mathrm{th}} = \left(TS_T \left(\frac{\partial \mu}{\partial \Phi} \right)_{P,T} - T \left(\frac{\partial \mu}{\partial T} \right)_{P,\Phi} + \mu \right) \mathbf{J}_m - \kappa \boldsymbol{\nabla} T, \tag{3.2}$$

where the coefficients D_m, S_T, μ, and κ are, respectively, the particle diffusion coefficient, the Soret coefficient, the

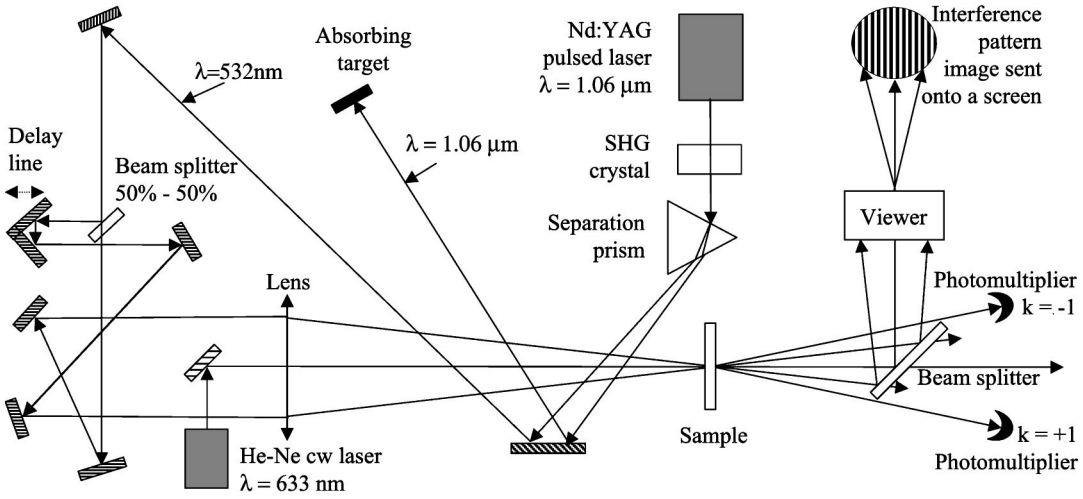

FIG. 1. Experimental forced Rayleigh scattering setup.

chemical potential of the colloid per unit volume, and the thermal diffusivity of the colloid. The following definition of the volume-fraction flow:

$$\mathbf{J}_m = \Phi \mathbf{v}, \tag{3.3}$$

where $\mathbf{v}$ is the particle mean velocity, is taken in the above equations. As the asymmetry between nanoparticles and solvent is very strong in ferrofluids, the notion of volume-fraction flow loses meaning as $\Phi \to 1$. The sometimes quoted following definition, $\mathbf{J}_m = \Phi(1-\Phi)\mathbf{v}$, is useless here as no study is made here beyond $\Phi = 8\%$. Equations (3.1) and (3.2) derive, with some changes, from those given by Landau and Lifshitz [Eqs. (58.11) and (58.12) in Ref. [22]. In addition to notation changes, and to a simplification due to constancy of pressure, a dielectrophoretic nanoparticle volume-fraction flow is present in Eq. (3.1). It is the product of Φ by the particle drift velocity [Eq. (3.3)] that is itself the product of the dielectrophoretic force $(-\boldsymbol{\nabla} U_d)$ by $D_m/k_B T$, i.e., the nanoparticle mobility according to the Stokes-Einstein relation. The dielectrophoretic force derives from the following potential:

$$U_d = -\frac{1}{2} V_d^* \varepsilon_0 E^2 = -Z_d I_p, \tag{3.4}$$

where E is the amplitude of the pump electromagnetic field, and V_d^* is an effective volume given by a Clausius-Mossotti-like relation [23]. It gives

$$Z_d = \frac{V_d^*}{2 n_p c} = \frac{3V}{2 n_p c} \frac{(n_p^n)^2 - (n_p^s)^2}{2 + (n_p^n)^2/(n_p^s)^2}, \tag{3.5}$$

where n_p is the real part of the refractive index of the colloid at the pump wavelength λ_p, c is the velocity of light, V is the mean nanoparticle volume, and n_p^n and n_p^s are the refractive indices, at λ_p, of the nanoparticle and of the solvent, respectively. The dielectrophoretic force is proportional to the gradient of the pump-beam intensity I_p inside the sample [see Eq. (3.4)].

In the absence of convection phenomena [see Eq. (57.2) of Ref. [22] for the first one], the following conservation equations complement Eqs. (3.1) and (3.2):

$$\frac{\partial \Phi}{\partial t} + \operatorname{div} \mathbf{J}_m = 0, \tag{3.6}$$

$$\rho c_p \frac{\partial T}{\partial t} + \operatorname{div} \mathbf{J}_{\mathrm{th}} = \dot{Q}, \tag{3.7}$$

where ρ is the mass density of the colloid, c_p its specific heat capacity, and $\dot{Q}$ is the heat input per unit time per unit volume of the colloid, due to the absorption of the pump laser beams. Finally $\mathbf{J}_{\mathrm{th}}$ and $\mathbf{J}_m$ obey boundary conditions on the cell walls, that will be detailed later on, when modeling processes in the FRS setup.

The coupling of Φ and T in Eqs. (3.1), (3.2), (3.6), and (3.7) makes a general solution in Φ and T difficult to be obtained. We propose hereafter an approximate solution, similar to that of Born and Oppenheimer, based upon the fact that, in colloids, thermal responses are much shorter ($\approx 10^{-4}$ s) than mass-diffusion processes (≈ 1 s). This approximation is easily validated if the pump-beam intensity I_p and hence $\dot{Q}$ and U_d are either time constant or periodic with a period δt much shorter than the mass-diffusion response time. In a first step of the approximation procedure, the fast evolution of temperature $T(\mathbf{r},t)$ in the magnetic colloid and in the cell is determined by regarding the particle volume fraction as a constant. It means that $\mathbf{J}_m$ is taken to be zero in Eq. (3.2) and that the volume fraction $\Phi(\mathbf{r},t)$ used implicitly in Eqs. (3.2) and (3.7) is ''self-consistently'' taken as a time-constant profile equal to $\Phi(\mathbf{r},t')$ in which t' lies in the time range in which temperature is determined. This gives

$$\frac{\partial T}{\partial t} - D_{\mathrm{th}} \Delta T = \frac{\dot{Q}}{\rho c_P}, \tag{3.8}$$

where D_{th} is the thermal diffusivity expressed as

$$D_{\mathrm{th}} = \kappa / \rho c_P. \tag{3.9}$$

In a second step, the slow time evolution of the volume fraction $\Phi(\mathbf{r},t)$ is found as a function of time t, through the following modified version of Eq. (3.1) in which T is changed into the time-averaged value $\langle T\rangle(\mathbf{r},t)$ of $T(\mathbf{r},t')$ in the vicinity of t, so that

$$\frac{\partial\Phi}{\partial t}-D_m\Delta\Phi=D_m(S_T\Delta\langle T\rangle+\varphi\Delta\langle U_d\rangle), \qquad (3.10)$$

with

$$\varphi=\Phi/k_B\langle T\rangle. \qquad (3.11)$$

As U_d varies even faster than T, the same averaging of U_d is made as with T. The function $\Phi(\mathbf{r},t)$ found must not depend on the detail of the time averaging of T and U_d. For the sake of simplicity, the following floating-time averaging of a function $f(t)$, is chosen:

$$\langle f\rangle(t)=1/t_a\int_t^{t+t_a}f(t')dt', \qquad (3.12)$$

where the averaging duration t_a lies between the thermal and mass-diffusion response times. In the case of a time-periodic pumping, t_a is chosen to be equal to the pump laser period δt.

As will be shown later on, no general solution of Eqs. (3.8) and (3.10) is needed in this work, as we only want to determine D_m and S_T. Therefore, measurements will be made on two different states of the sample that are briefly described hereafter. For the evaluation of S_T, it is noticed that, if the pump-laser light intensity is time periodic, $\Phi(\mathbf{r},t)$ becomes independent of t long after the pump laser has been switched on. Denoting by $\Phi(\mathbf{r})$ the function $\Phi(\mathbf{r},t=\infty)$, Eq. (3.1) reduces to

$$\boldsymbol{\nabla}\Phi+S_T\boldsymbol{\nabla}\langle T\rangle+\varphi\boldsymbol{\nabla}\langle U_d\rangle=\mathbf{0}. \qquad (3.13)$$

This regime, called "*steady state*" further in this paper, is well suited for studying the two-time-scale model. The above equation will be used to derive S_T and the dielectrophoretic contribution.

For evaluating D_m, we will use the fact, included in the two-time scale model, that temperature becomes very quickly homogeneous in the sample after the pump laser beams have been switched off. When temperature homogeneity is achieved, Eq. (3.10) reduces to the following well-known diffusion equation:

$$\frac{\partial\Phi}{\partial t}-D_m\Delta\Phi=0. \qquad (3.14)$$

This regime, called "*decay state*" further in this paper, has already been studied by the present authors [5,8,13]. Finally, we will use linearized versions of these last two equations by taking coefficients S_T, φ, and D_m, as constants.

IV. LINEARIZED TWO-DIMENSIONAL APPROXIMATION

The two-time-scale model is tested in a simple geometry in which FRS experiments are idealized by assuming a two-dimensional (2D) infinite extension for the interference pattern of the two pump beams. The sample is a thin layer of magnetic colloid located between two glass plates that define a (Ox,Oy) plane, the (Oy) axis being parallel to the fringes. The mean direction of the pump beams is orthogonal to the sample plane and defines the (Oz) axis. The ferrofluid sample lies in the region $0<z<l$, whereas the input and output cell glass plates of thickness e correspond to the zones $-e<z<0$ and $l<z<l+e$, respectively. For a contrast γ in the interference pattern of the two pump beams, the light intensity can be approximated to

$$I_p(x,y,z,t)=I_p^0(t)[1+\gamma\cos(qx)]\exp(-a_pz), \qquad (4.1)$$

where $I_p^0(t)$ is the mean intensity of the pump beams, and a_p is the absorption coefficient at the pump wavelength λ_p. The wave vector q of the interference pattern is defined by

$$q=2\pi/\Lambda, \qquad (4.2)$$

where the interfringe length Λ is expressed as

$$\Lambda=\frac{\lambda_p}{2\sin(\theta/2)}, \qquad (4.3)$$

for an angle θ between the two pump-beam directions; Λ is also the spatial period of the grating generated in the sample.

To complete this two-dimensional approximation, Φ, T, and all the other thermodynamic variables are assumed not to depend on y and to be periodic along the (Ox) direction, giving rise to the diffraction phenomenon. As Eqs. (3.8), (3.10), and (3.13) are assumed to be linear, and as the Fourier expansion of the light intensity I_p in Eq. (4.1) is limited to the first order in $\cos(qx)$, the expansions of T and Φ are limited to the first order, too. In the absence of an interference pattern, the glass plates and the colloidal sample are homogeneous and isotropic in the (Ox, Oy) plane; therefore, T and Φ exhibit no spatial dephasing with respect to the interference pattern, and no $\sin(qx)$ term appears in their expansions:

$$T(x,y,z,t)=T_0(z,t)+T_1(z,t)\cos qx, \qquad (4.4)$$

and

$$\Phi(x,y,z,t)=\Phi_0(z,t)+\Phi_1(z,t)\cos qx. \qquad (4.5)$$

Ten to twenty fringes are seen in the interference pattern, which is enough to validate a model where a x periodicity is assumed for T and Φ.

The determination of the function T should be done by solving Eq. (3.7), noticing that

$$\dot{Q}(x,y,z,t)=a_pI_p(x,y,z,t). \qquad (4.6)$$

For a rigorous description of the diffracted intensity of the probe beam, the temperature variations inside the glass plates

of the cell should be taken into account as well as those inside the colloid. As the aim of this paper is not the mathematical determination of T, but that of Φ as a function of T, we will just check the characteristics of T that are to be measured. In the following reasoning, both functions $T_0(z,t)$ and $T_1(z,t)$ are assumed to be already known.

In the steady-state regime, Eq. (3.13) becomes

$$\frac{\partial \Phi(x,z)}{\partial x} + S_T \frac{\partial \langle T(x,z,t)\rangle}{\partial x} + \varphi \frac{\partial \langle U_d(x,z,t)\rangle}{\partial x} = 0, \quad (4.7)$$

which gives the following relations between the $\cos(nqx)$ $(n=0,1)$ Fourier components of Φ, T and U_d:

$$\Phi_0(z) + S_T \langle T_0(z,t)\rangle + \varphi \langle V_{d0}(z,t)\rangle = K, \quad (4.8)$$

where K is independent of position, and

$$\Phi_1(z) + S_T \langle T_1(z,t)\rangle + \varphi \langle U_{d1}(z,t)\rangle = 0. \quad (4.9)$$

The definitions of U_{d0} and U_{d1} are similar to those of T_0 and T_1 in Eq. (4.4).

In the decay-state regime, $\partial\Phi/\partial z$ is zero at $z=0$ and $z=l$, because there is no drift (Soret effect and dielectrophoresis) term in Eq. (3.14). To make the determination of Φ easier in this regime, its domain of definition is extended to $[-\infty, +\infty]$ by assuming Φ to be symmetric with respect to $z=0$ and $z=l$. The extended function Φ is continuous and $2l$-periodic, allowing the following Fourier expansion of $\Phi_{j_x}(z,t)$ along z:

$$\Phi_{j_x}(z,t) = \sum_{j_z \geqslant 0} \Phi_{j_x j_z}(t) \cos(j_z q_z z), \quad (4.10)$$

with $j_x = 0$ or 1, and

$$q_z = \pi/l. \quad (4.11)$$

Equation (3.14) gives

$$\Phi_{j_x j_z}(t) = \sum_{j_x j_z} \Phi_{j_x j_z} \exp(-t/\tau_{m j_x j_z}), \quad (4.12)$$

where the mass-diffusion time constant $\tau_{m j_x j_z}$ is expressed as

$$\tau_{m j_x j_z}{}^{-1} = D_m (j_x{}^2 q^2 + j_z^2 q_z^2). \quad (4.13)$$

As the system is assumed to be infinite along (Ox) and (Oy), the mean value Φ_{00} of Φ, defined by

$$\Phi_{00} = \frac{1}{l} \int_0^l \Phi_0(z)\, dz, \quad (4.14)$$

does not vary with time because of particle-number conservation, which is consistent with Eq. (4.13). With an actual finite-size laser spot, it would not be exactly the case.

V. EXPERIMENTAL DETERMINATION OF THE TEMPERATURE RESPONSE AND EVIDENCE FOR A CONCENTRATION GRATING

In the following, the study is mostly restricted to the so-called steady-state regime. This restriction does not prevent the most important parameters of the two-time-scale model from being evaluated if the temperature and volume-fraction responses are clearly distinguishable from each other in the experimental diffraction signal.

A time-independent analysis of the different contributions to the diffracted signal is given in the Appendix. In its final expression (A7), the ratio of the first-order diffracted intensity to the transmitted one, $I_d^{k=1}/I_d^{k=0}$, is related to the following z averages of Fourier components:

$$T_{F1} = \frac{1}{l} \int_0^l T_1(z)\, dz, \quad (5.1)$$

$$\Phi_{F1} = \frac{1}{l} \int_0^l \Phi_1(z)\, dz, \quad (5.2)$$

$$T_{G1} = \frac{1}{l} \left(\int_{-e}^{0} T_1(z)\, dz + \int_l^{l+e} T_1(z)\, dz \right), \quad (5.3)$$

through partial derivatives of the refraction indices $n'_F + i n''_F$ and n'_G of the ferrofluid and the cell glass, respectively. The imaginary part of the refraction index of the magnetic colloid ($n''_F \approx 10^{-3}$) is much less than unity, which makes, in Eq. (A8), $\partial n''_F/\partial T$ and $\partial n''_F/\partial\Phi$ quite negligible in front of $\partial n'_F/\partial T$ and $\partial n'_F/\partial\Phi$, respectively (in the CX207BNE sample we have found $(\partial n''_F/\partial T) \approx 2 \times 10^{-6}\ \mathrm{K}^{-1}$, $(\partial n''_F/\partial\Phi) \approx 10^{-2}$, $\partial n'_F/\partial T = -5.6 \times 10^{-4}\ \mathrm{K}^{-1}$, and $\partial n'_F/\partial\Phi = 1.08$). Therefore Eq. (A7) reduces to

$$I_d^{k=1}/I_d^{k=0} = \left(\frac{\partial n'_F}{\partial T} 2\pi l/\lambda_t \right)^2 [T_{F1}(t) + r T_{G1}(t) - N^F \Phi_{F1}]^2, \quad (5.4)$$

where the ratios r and N^F are defined by

$$r = \frac{\partial n'_G}{\partial T} \Big/ \frac{\partial n'_F}{\partial T}, \quad (5.5)$$

and

$$N^F = -\frac{\partial n'_F}{\partial \Phi} \Big/ \frac{\partial n'_F}{\partial T}. \quad (5.6)$$

The "calibration factor" N^F, so defined, has the dimension of a temperature and is positive if $\partial n'_F/\partial T$ is negative, as is usually the case.

As seen above T and Φ modulations extend on at least ten Λ periods along (Ox). The probe beam is broad enough to be diffracted by the whole temperature and concentration grating, which is enough for detecting it. In fact, diffracted beams ($k = \pm 1$ and sometimes ± 2) are visually observed as round spots on a screen. Let us examine now the qualitative

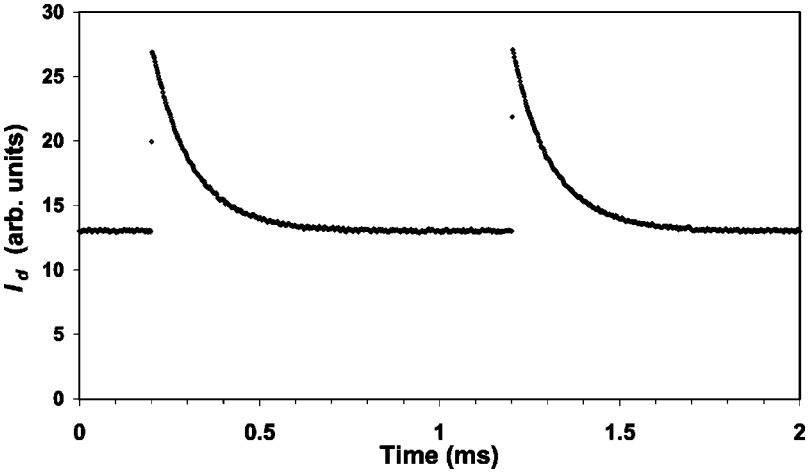

FIG. 2. Typical fast response of the first-order diffracted intensity. Measurements are performed at a fixed pulse-repetition rate of 1 kHz in a sample of BNE-surfacted maghemite in cyclohexane (CX207BNE, $\Phi=3.3\%$) with a cell thickness of 10 μm and a grating period of 28 μm. The curve clearly shows a continuous background due to a concentration grating and a transient contribution due to a temperature grating.

features of the experimental diffracted intensity as a function of time in the case of CX207BNE samples. The two expected types of contributions are easily distinguished in the curves of Fig. 2. The transient thermal contribution is recognized as an instantaneous increase of the diffracted intensity, followed by an exponential relaxation, whereas the continuous background is due to the constant-concentration contribution. Diffraction signals are rather noisy and have to be averaged over tens or hundreds of similar experiments. Finally, it is observed that all experimental curves can be fitted to

$$I_d^{k=1}(t)=G\left(e^{-t/\tau}+X\right)^2, \tag{5.7}$$

with a very good precision, between two consecutive laser pulses; for the sake of simplicity, the starting time of a pump pulse is assumed to be $t=0$ in Eq. (5.7). This procedure simultaneously provides accurate values for G, τ, and X. Quantities G and τ are strictly positive whereas, as will be shown further, the sign of X depends on the characteristics of the studied colloid. As a preliminary remark, it is worth noticing that the discontinuity of $I_d^{k=1}$ at $t=0$ in Eq. (5.7) implies that the power input $I_p^0(t)$ can be approximated as a set of delta functions; this is expected since typical sample response times are larger than the duration of each laser pulse. To prove the consistency of the two-time-scale model from the experimental observation delivering Eq. (5.7), a two-step reasoning is chosen. In the first step, it is shown that the observed exponential decay has a thermal origin. In the second step, the constant contribution X is shown to be due to a steady spatial modulation of the volume fraction.

By varying the angle θ between the interfering beams, it is observed that τ obeys

$$\tau^{-1}={\tau_0}^{-1}+Dq^2, \tag{5.8}$$

where τ_0 and D are constant (Fig. 3). This phenomenological law proves the diffusive origin of the decay. In addition, the values found for D in all the studied samples are roughly equal to the thermal diffusivity $D_{\rm th}$ of the magnetic colloids at the volume fraction Φ. For instance, in the 3.3% CX207BNE sample, D is found to be 1.1×10^{-7} m^2 s^{-1} while Eq. (3.9) gives $D_{\rm th}=0.80\times10^{-7}$ m^2 s^{-1} with $\kappa=0.123$ W m^{-1} K^{-1}, and $\rho c_p=1.54\times10^6$ J m^{-3} K^{-1} [24,25]. The observed decay is, therefore, mostly due to heat diffusion in the colloid. Generally speaking, thermal responses are series expansions of exponential decays, but in the measurements reported here only one term is detected, which allows us to denote henceforth by $\tau_{\rm th}$ the decay time τ. A second point is worth noticing: thermal effects in glass plates give no detectable contribution to the diffraction signal. Two converging explanations can be advanced for the lack of contribution due to the glass plate. The first one is that, as the proper response time of the glass plates is much shorter than that of the colloid layer, $T_{G1}(t)$ is "forced" by $T_{F1}(t)$, and then should exhibit the same decay profile as $T_{F1}(t)$. The second explanation is that the product $r\,T_{G1}(t)$ can be neglected in front of $T_{F1}(t)$ in Eq. (5.4), firstly because r is much lower than unity ($r=3\times10^{-5}/5\times10^{-4}=6\times10^{-2}$ [see Eq. (5.5)]), and secondly because $T_{G1}(t)$ should be much smaller than $T_{F1}(t)$. Two reasons can be brought for the last assertion: (i) the glass plates behave, more or less, like thermal short circuits because the thermal diffusivity of fused silica glass (1.35 W m^{-1} K^{-1}) is about eleven times larger than that of the magnetic colloids, and (ii) the thermal conductance through the glass-colloid interface decreases the

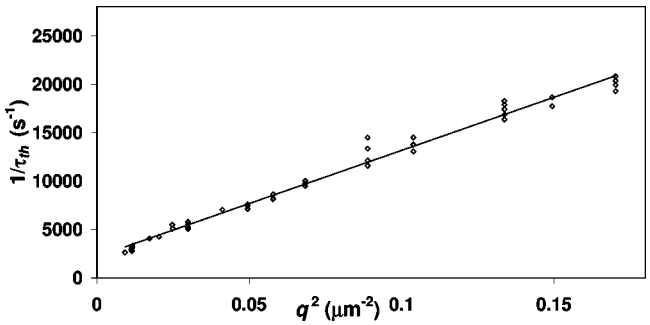

FIG. 3. Linearity of the thermal decay constant $1/\tau_{\rm th}$ as a function of the squared grating wave vector q^2. Measurements are performed in a sample of BNE-surfacted maghemite in cyclohexane (CX207BNE, $\Phi=3.3\%$) with a cell thickness of 20 μm. The best-fit slope (1.1×10^{-7} m^2 s^{-1}) is close to the estimated thermal diffusivity in the colloid ($D_{\rm th}=0.8\times10^{-7}$ m^2 s^{-1}), thus proving the thermal origin of the fast decay. The same best-fit procedure gives a time constant $\tau_0=0.46$ ms at $q=0$.

space-periodic heat flow in the glass plates. Neglecting the r $T_{G1}(t)$ contribution in Eq. (5.4), $T_{F1}(t)$ can then be simplified to

$$T_{F1}(t)=T_{F1}^0 e^{-t/\tau_{\rm th}}, \tag{5.9}$$

where T_{F1}^0 is a temperature amplitude to be determined later. The average value $\langle T_{F1}\rangle$ of $T_{F1}(t)$ is thus given by

$$\langle T_{F1}\rangle = T_{F1}^0 \frac{\tau_{\rm th}}{\delta t}[1-\exp(-\delta t/\tau_{\rm th})], \tag{5.10}$$

where δt is the pump-pulse repetition period. In the framework of a single thermal response time due to the colloid only, Eq. (5.4) reduces then to

$$I_d^{k=1}/I_d^{k=0}=\left(\frac{\partial n'_F}{\partial T}T_{F1}^0 2\pi l/\lambda_t\right)^2\left(e^{-t/\tau_{\rm th}}-N^F\frac{\Phi_{F1}}{T_{F1}^0}\right)^2. \tag{5.11}$$

By identifying this two-time-scale-model equation with the phenomenological one (5.7), the following expression is found for T_{F1}^0:

$$T_{F1}^0=\frac{\lambda_t}{2\pi l}\sqrt{\frac{G}{I_d^{k=0}}}\Big/\frac{\partial n'_F}{\partial T}. \tag{5.12}$$

The accuracy of the value of T_{F1}^0 given by this expression is rather poor, as transmitted and diffracted light intensities are measured separately along different beam directions, and in addition they differ by several orders of magnitude. Another estimation of T_{F1}^0 from physical properties of the samples is given at the end of Sec. VI.

By the same identification procedure, the following relation is found between X and the ratio Φ_{F1}/T_{F1}^0:

$$X=-N^F\Phi_{F1}/T_{F1}^0. \tag{5.13}$$

The ratio Φ_{F1}/T_{F1}^0 is determined with a good accuracy, as it is determined from only one averaged diffraction curve, and it is calibrated by the amplitude of the thermal contribution. For a precise measurement of the discontinuity in the diffracted intensity at a pulse input time, and for a good analysis of the decay of the temperature grating, the delay between two consecutive pulses has to be larger than the thermal relaxation time $\tau_{\rm th}$. Furthermore, the volume fraction Φ must not vary significantly between two pulses for a valid use of the two-time-scale model. Therefore, δt has to obey $\tau_{\rm th}<\delta t<\tau_{m\ 10}$ [see Eq. (4.13)]. All the experiments presented hereafter are performed with a pulse-repetition rate

$$F=\delta t^{-1}, \tag{5.14}$$

ranging between 1 Hz and 1 kHz, as $\tau_{m\,10}$ and $\tau_{\rm th}$ are typically 10^{-1} and 10^{-4} s, respectively, (1.5 kHz is the upper limit of the pulse-repetition rate of our Nd:YAG laser). At $F=10$ Hz, the concentration contribution is hardly noticeable in the diffraction signal, whereas, at $F=1$ kHz, it is 10^4 times larger and is an important part of the signal.

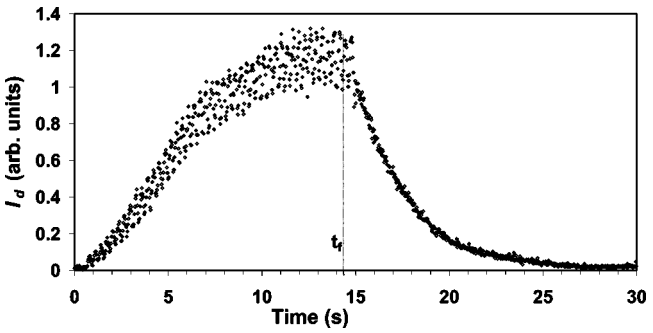

FIG. 4. Typical slow response of the first-order diffracted intensity as the pump laser is switched on and then off. Measurements are performed in a sample of BNE-surfacted maghemite in cyclohexane (CX207BNE, $\Phi=3.3\%$) with a cell thickness of 10 μm and a grating period $\Lambda=68$ μm. Pump beams are switched on at $t=0$ and switched off at $t=t_f$. During the heating duration ($0<t<t_f$) the temperature contribution follows the pump-light periodicity (see Fig. 2). Due to sampling processes in the measurement, the temperature contribution is observed here as a noise, whereas the concentration contribution is continuous. Saturation is observed when the concentration steady state is reached. When the pump beams are switched off ($t>t_f$), the thermal modulation disappears immediately (discontinuity in the diffracted intensity). The following exponential decrease of the diffracted intensity corresponds to the vanishing of the concentration grating.

The above condition on δt should also hold for studying a nonsteady-state concentration grating in the two-time-scale framework. The buildup process of the concentration grating once the pump laser is switched on, and its decay after the pump laser is switched off, can be studied with the same diffraction technique, but with a slower data acquisition device as measurements last some seconds. The temperature grating can still be observed in the first-order diffracted intensity curves; it is seen in Fig. 4 as a noise because the measurement is achieved by random sampling. The buildup of the concentration grating will not be studied here, and we henceforth focus on the fast steady-state measurement results and secondarily on the decay processes. Finally, the analysis can be extended, with some care, for studying steady-state responses to more complex time-periodic excitations than those given by our pulsed laser [13,26,27].

VI. EVIDENCE FOR A SORET EFFECT AND THE LACK OF DIELECTROPHORESIS

We are now in a position to evidence or disprove, under the experimental conditions described above, thermodiffusive or dielectrophoretic effects in magnetic colloids. More precisely, in this section is described the determination of S_T and Z_d from a set of experimental data, within the framework of the linearized two-time-scale model. Actually the order of magnitude of Z_d could be calculated from relation (3.5), but we prefer to leave it as an unknown parameter to be experimentally determined together with S_T. It will be proved from the linear model, and confirmed experimentally, that both values do not depend on the laser peak power.

According to our linearized transport model [Eq. (4.9)],

and using Eqs. (5.1), (5.2), (3.4), and (4.1), the amplitude Φ_{F1} of the concentration grating is also expressed as

$$\Phi_{F1}=-\left(S_T\langle T_{F1}\rangle-\gamma\varphi Z_d\langle I_p^0\rangle\frac{1}{l}\int_0^l\exp(-a_pz)dz\right). \tag{6.1}$$

As X, the constant contribution to the measured diffracted signal [Eq. (5.7)], is related to Φ_{F1} by means of Eq. (5.13), it can be written as the following linear combination of the Soret coefficient S_T and of the dielectrophoretic factor Z_d:

$$X=N^F\left\{S_T[1-\exp(-1/F\tau_{\rm th})]F\tau_{\rm th}-Z_d\gamma\varphi\frac{\langle I_p^0\rangle}{T_{F1}^0}\frac{1-\exp(-la_p)}{la_p}\right\}, \tag{6.2}$$

using Eqs. (5.10), (5.13), (5.14), and (6.1). In the above expression, the Soret term does not depend on $\langle I_p^0\rangle$. Nor does the dielectrophoretic one as $\langle I_p^0\rangle$ is proportional to T_{F1}^0 as we proceed to show. The energy $\langle I_p^0\rangle\delta t$ of each pump-laser pulse warms up the colloid instantly by an amount determined from Eqs. (3.8) and (4.6). The normalized integral on the colloid thickness of its first Fourier component along (Ox), is expressed as follows:

$$T_{F1}(t=0^+)-T_{F1}(t=\delta t^-)=\langle I_p^0\rangle\frac{\gamma\delta t}{l\rho c_p}[1-\exp(-la_p)]. \tag{6.3}$$

In the above equation the left-hand side is the discontinuity of $T_{F1}(t)$ at $t=0$ [Eqs. (5.9) and (5.1)]. The proportionality of $\langle I_p^0\rangle$ to T_{F1}^0 is then proved [see Eq. (5.14)], namely,

$$\frac{\langle I_p^0\rangle}{T_{F1}^0}=\frac{Fl\rho c_p}{\gamma}\frac{1-\exp(-1/F\tau_{\rm th})}{1-\exp(-la_p)}. \tag{6.4}$$

Equation (6.2) then simplifies to

$$X=F[1-\exp(-1/F\tau_{\rm th})]N^F(S_T\tau_{\rm th}-P), \tag{6.5}$$

where the dielectrophoretic coefficient P is defined by

$$P=Z_d\varphi\rho c_p/a_p. \tag{6.6}$$

In the above expression for X, the presence of $\tau_{\rm th}$ through the product $S_T\tau_{\rm th}$ makes a clear distinction between S_T and P. It reminds that the Soret effect arises from the persistency of the temperature grating, whereas dielectrophoresis is due to the instantaneous electromagnetic power input.

The next step of the reasoning is devoted to verifying, on a set of experiments made on the same sample, that F, X, and $\tau_{\rm th}$ obey relation (6.5). By ''sample'' we mean here a specific magnetic colloid, with a given volume fraction Φ, in a cell of definite thickness l. As previously, the study is performed on the CX207BNE ferrofluid at $\Phi=3.3\%$ (i.e., Φ_{00} according to our notation). For ease of presentation, let us introduce

$$X^*=X/[1-\exp(-1/F\tau_{\rm th})], \tag{6.7}$$

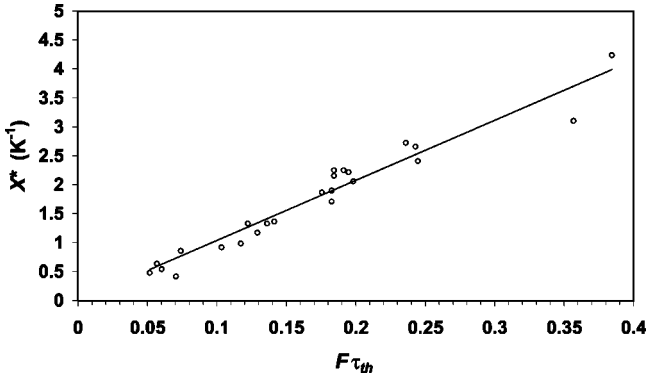

FIG. 5. Proportionality of the normalized concentration modulation X^* to the relaxation time $\tau_{\rm th}$. Measurements are performed at a fixed pump-pulse-repetition rate $F=1$ kHz in a sample of BNE-surfacted maghemite in cyclohexane (CX207BNE, $\Phi=3.3\%$) with a cell thickness of 20 μm. X^* is plotted as a function of the product $F\tau_{\rm th}$. The best-fit line crosses the origin, which evidences the lack of dielectrophoresis; its slope, 10.3 K^{-1}, is equal to the product N^FS_T.

instead of X. The $F\tau_{\rm th}$ correction shows that the more incomplete the thermal relaxation between two consecutive pulses, the more persistent the temperature modulation, and the more contrasted the concentration grating. In our model X^* is expressed as

$$X^*=FN^F(S_T\tau_{\rm th}-P). \tag{6.8}$$

The factor X^* is easily connected to an experimental intensity ratio R through

$$X_\pm^*=\frac{\pm1}{R\mp1}\frac{1\mp R\exp(-1/F\tau_{\rm th})}{1-\exp(-1/F\tau_{\rm th})}, \tag{6.9}$$

where R is defined by

$$R=\sqrt{\frac{I_d^{k=1}(t=0^+)}{I_d^{k=1}(t=0^-)}}. \tag{6.10}$$

In Eq. (6.9) the upper sign stands for the case of a $I_d(t)$ curve without any zero ($X<-1$ or $0<X$), whereas the lower sign stands for the case of a $I_d(t)$ curve with one zero ($-1<X<0$) [see Eq. (5.7)]. Using Eq. (6.8), the determination of S_T and P can be achieved by studying separately the dependence of X^* on the heat diffusion time $\tau_{\rm th}$ (keeping F constant) and the dependence of X^* on the heat input rate F (keeping $\tau_{\rm th}$ constant).

In Fig. 5, X^* is plotted as a function of the product $F\tau_{\rm th}$, where $\tau_{\rm th}$ is varied by changing the interference angle θ [Eqs. (4.3) and (5.8)], whereas F is fixed at a high value (1 kHz) so as to get the most contrasted signal. Results are obtained with a 20 μm thick, $\Phi=3.3\%$ CX207BNE sample. All the experimental points fall, to a good approximation, along a straight line whose equation is identified with Eq. (6.8), and the product N^FS_T is determined by the slope value. The identification gives a second important information: within the experimental uncertainty range, $P=0$, and the same zero value is found for P in all the CX207BNB-type samples.

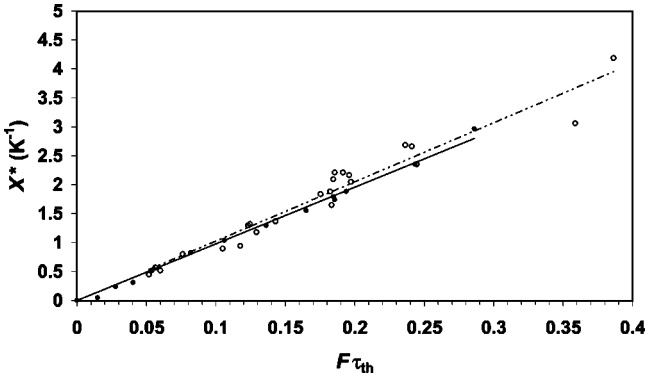

FIG. 6. Proportionality of the normalized concentration modulation X^* to the repetition rate F. Measurements are performed by varying the pulse-repetition rate F from 1 Hz to 1 kHz at a fixed interfringe of 45 μm (fixed thermal relaxation time, $\tau_{\text{th}}=0.29$ ms) in a sample of BNE-surfacted maghemite in cyclohexane (CX207BNE, $\Phi=3.3\%$) with a cell thickness 20 μm (●). X^* is plotted as a function of the product $F\tau_{\text{th}}$. The point near the origin is experimental. Points obtained by varying τ_{th} at fixed F, and already given in Fig. 5, are also shown in Fig. 6 (○), which proves the consistency of both plots ($N^F S_T=9.7\ \text{K}^{-1}$).

Fixing now the temperature decay time τ_{th}, F is varied from 1 Hz to 1 kHz the corresponding plots of X^* as a function of the product $F\tau_{\text{th}}$ are shown in Fig. 6 with the same $\Phi=3.3\%$, 20-μm-thick CX207BNE sample as above. The points fall along a straight line that passes through the origin in accordance with Eq. (6.8). As P has been shown above to be zero, both plots obtained by varying either τ_{th} or F, are equivalent, and the same value is found for the product $N^F S_T$ (9.7 K^{-1}). For a better proof, the plot given in Fig. 5 is given again in Fig. 6. The two-time-scale model provides a reliable value for $N^F S_T$, which does not depend on the way τ_{th} is related to experimental parameters. The highest precision in the determination of $N^F S_T$ is obtained when terms of both origins have similar orders of magnitude. It is the reason why surfacted maghemite in cyclohexane (CX207BNE sample) was chosen to test this method of determination of P and S_T; cyclohexane, as a solvent, yields a value for $\partial n'_F/\partial T$ which is about four times larger than that in water, which makes the two contributions very easily distinguishable from each other in the diffracted signal. A second reason for choosing this material lies in the low absorption coefficient of maghemite, compared to that of cobalt ferrite, at the probe He-Ne laser wavelength.

The dielectrophoretic effect is overwhelmed by the observed large thermodiffusive one, although, for a long time, the former was thought to be the main mechanism in the buildup process of concentration gratings in magnetic colloids [5,8]. In fact, the only effect giving rise to concentration gratings is the temperature modulation. The lack of dielectrophoresis is theoretically not very surprising because, if P is determined from expressions (6.6), (3.5), and (3.11), $P=0.307\times10^{-12}\ \text{s K}^{-1}$ is found for the CX207BNE colloid at room temperature (with $n_p^n=2.61$, $n_p^s=1.4266$, $n_p=1.462$, and $a_p=5.775\times10^4\ \text{m}^{-1}$ and data from Sec. VI, Table I, and Ref. [24]). As N^F is 1929 K (Table II), and the thermal response time τ_{th} about 10^{-4} s, the dielectrophoresis coefficient P is negligible compared to the Soret term $S_T\tau_{\text{th}}$ ($\approx10^{-6}\ \text{s K}^{-1}$) in the evaluation of X^* through Eq. (6.8).

Although our method for determining S_T is independent of the pump intensity, the input level has to be low enough to ensure linearity. The Soret data obtained can be validated by

TABLE II. Calibration factor and reduced Soret parameters in the magnetic colloids under study. The calibration factor N^F is the opposite of the ratio of the two partial derivatives $\partial n_F/\partial T$ and $\partial n'_F/\partial\Phi$ of the refractive index n'_F of the ferrofluid. They are determined from measurements made with a total-refraction refractometer (no uncertainty range is given here). Reduced Soret parameters, i.e., Soret data that are independent of the dilution rate. The reduced concentration contribution X_T^*, defined in Eq. (7.4), is the first reduced Soret parameter to be determined. Many consistent experiments have been performed in CX207BNE and V207NO3 samples. Less experimental results have been collected in the other four samples, leading to an uncertainty range much larger than in the first two. The reduced Soret coefficient S_T^* is found from X_T^* and N^F through Eq. (7.5). It characterizes, when multiplied by T, the Soret-force response to a temperature gradient. The Soret mobility μ_S is found through Eq. (7.7) from S_T^* and D_m. It characterizes the Soret-velocity response to a temperature gradient. Symbol ≈ before a number indicates a value estimated from nearby data.

Sample name	$10^4\frac{\partial n'_F}{\partial T}$ (K^{-1})	$\frac{\partial n'_F}{\partial\Phi}$	N^F (K)	X_T^*	$10^3 S_T^*$ (K^{-1})	$10^{12} D_m$ ($\text{m}^2\,\text{s}^{-1}$)	$10^{-9}\mu_S$ ($\text{kg}^{-1}\,\text{s}$)
Surfacted							
CX207BNE	−5.6	1.08	1929	320±60	166±31	30.6±5	368±129
Tol207BNE	−5.6	1.08	1929	280±80	145±41	≈51	536±237
CX207OA	−5.6	1.08	1929	56.5±9	29±5	≈30.6	≈64
Ionic							
V207NO3	−1.22	1.32	10 820	−820±150	−76±14	36±5	−198±64
V207Cit	−1.22	1.32	10 820	−2000±1000	−185±92	21±6	−282±150
S184			≈10 820	−5000±2000	≈−462	≈17.3	≈−579

considering the maximum of the temperature increase in the sample with respect to the room temperature. This quantity is determined at the center of the interference-pattern immediately after each pump pulse ($t=0^+$) and is approximated as the sum of two contributions. The first one is the amplitude, T^0_{F1}, of the space modulation (neglecting here the z variation in thin samples) of the temperature increase due to the interference of the two pump beams [Eq. (5.9)]. T^0_{F1} is estimated from Eq. (6.4), and not from Eq. (5.12) as G is not determined here. The second contribution, without any space modulation, is the temperature increase that the two pump beams would yield in the absence of interference. A precise thermal model is beyond the aim of this paper, but it is estimated as the value at $t=0^+$ of a periodical (δt) temperature increase that decays with a exponential decay time τ_0 [Eq. (5.8) with an infinite grating step Λ] and that has a discontinuity of $\langle I^0_p\rangle \delta t[1-\exp(-la_p)]/l\rho c_p$ at $t=0$ similar to that seen in Eq. (6.3). Upper limits for both terms are found with $\gamma=1$, $F=1$ kHz, $\langle I^0_p\rangle=15$ mW, and $l=20$ μm. For a 3.3% CX207BNE surfacted sample ($\tau_0=0.455$ ms) and with an experiment leading to $\tau_{\rm th}=0.29$ ms, we find 2.74 and 2.98 °C for the upper limits to the first and second contributions, respectively. As ρc_p is about three times larger in water than in cyclohexane, both temperature increases are about three times less with ionic samples than with surfacted ones. Overheating is, therefore, shown to be low enough so that linearity holds good; it is even more credible if the second one is just considered as a sample-temperature shift. Similarly Eqs. (6.1) and (5.10) give $\Phi_{F1}<4.2\times10^{-3}$ keeping the model linearity.

VII. PARTICLE ORIGIN OF THE SORET EFFECT AND ALGEBRAIC SORET PARAMETERS

All the experimental results presented up to now come from the same CX207BNE surfacted magnetic colloid because this material gives the best measurements for applying our analysis. Now we are in a position to focus on general properties of the Soret effect in ferrofluids. For this purpose, samples of six different natures, three surfacted and three ionic, will be studied. As a preliminary remark, let us note that S_T can now be determined by a shorter method than that given in Sec. VI. In fact, the expressions used to determine P have a dielectric origin and are based on properties of the nanoparticle core, not on those of the stabilization coating. As the dielectric characteristics of nanoparticle cores cannot vary by orders of magnitude from one type to another [Eq. (3.5)], it is reasonable to extend the characteristics seen in the CX207BNE sample and set P to zero in all magnetic colloids. The Soret coefficient can then be determined from the following expression [see Eq. (6.8)]:

$$S_T=X^*/(F\tau_{\rm th}N^F). \tag{7.1}$$

In Fig. 7, X^* is plotted as a function of $F\tau_{\rm th}$ from FRS experiments on six ferrofluids ($\tau_{\rm th}$ kept constant for each one). We have chosen to show on the same figure two ways of determining the thermodiffusive properties of a sample using Eq. (7.1): (i) a complete one where many values of X^* and $F\tau_{\rm th}$ are measured, which provides a reliable best-fit value for the product N^FS_T, and (ii) a less accurate way where only one value of X^* and $F\tau_{\rm th}$ is measured, which gives only an estimated value of the product N^FS_T. In Fig. 7 are given a complete data set and two reduced data sets for each type of ferrofluid, surfacted and ionic. As N^F is known to be positive in all magnetic colloids, the most striking information conveyed by Fig. 7 is: (i) S_T is positive in all the surfacted ferrofluids we studied, so that nanoparticles move from warmer regions toward colder ones, and (ii) opposite results are observed in all the aqueous ionic ferrofluids we studied, which means that their Soret coefficient S_T is negative, and that nanoparticles move from colder regions to warmer ones. In other words, in surfacted ferrofluids, the diffracted field exhibits two contributions of the same sign ($X>0$, as seen in Fig. 2), temperature and concentration modulations have opposite phases [Eq. (5.4) with $r=0$], and S_T is positive. On the contrary, in ionic colloids the two contributions to the diffracted field have opposite signs ($X<0$), both modulations then have the same phases, and S_T is negative. These sign differences are particularly observed with samples that share the same maghemite core but differ in the stabilization (Table II). As a conclusion, the sign of the Soret coefficient depends only on the nature of the colloid stabilization of the ferrofluid, not on the core nature.

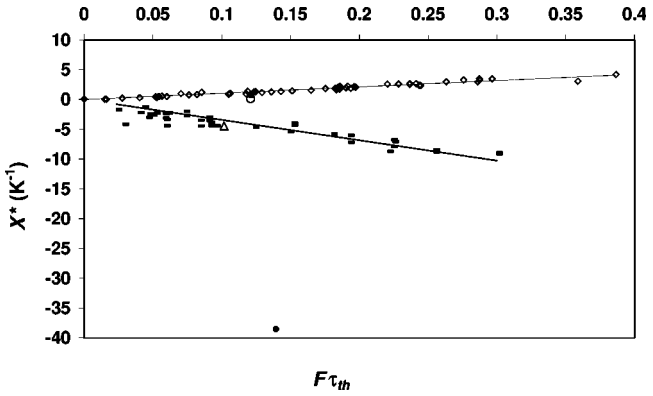

FIG. 7. Normalized concentration modulation X^* as a function of $F\tau_{\rm th}$ in different samples. Normalized concentration modulation X^* is plotted as a function of $F\tau_{\rm th}$ with a varied pulse-repetition rate F and a fixed relaxation time $\tau_{\rm th}$ for various samples: (◇) BNE-surfacted maghemite in cyclohexane (CX207BNE, $\Phi=3.3\%$), (▲) BNE-surfacted maghemite in toluene (Tol207BNE, $\Phi=3.3\%$), (○) oleic-acid-surfacted maghemite in cyclohexane (CX207OA, $\Phi=3.3\%$), (■) ionic noncitrated maghemite ($V207NO_3^-$, $\Phi=3.3\%$), (△) ionic citrated maghemite (V207Cit, $\Phi=3.3\%$), (●) citrated cobalt ferrite (S184, $\Phi=6\%$). The product N^FS_T is given by the slope of the best fit straight line crossing the origin [Eq. (7.1)]. The origin is an experimental point as no diffraction is observed at $F=0$ (no pumping and no permanent grating). The ionic or surfacted nature of the colloid is reflected in the sign of N^FS_T.

To finish with the complete determination of S_T according to Eq. (7.1), the calibration factor N^F needs to be known by evaluating the two partial derivatives $\partial n'_F/\partial\Phi$ and $\partial n'_F/\partial T$ [Eq. (5.6)]. For this purpose we have measured, at the probe wavelength, the real part of the refraction index n'_F of many

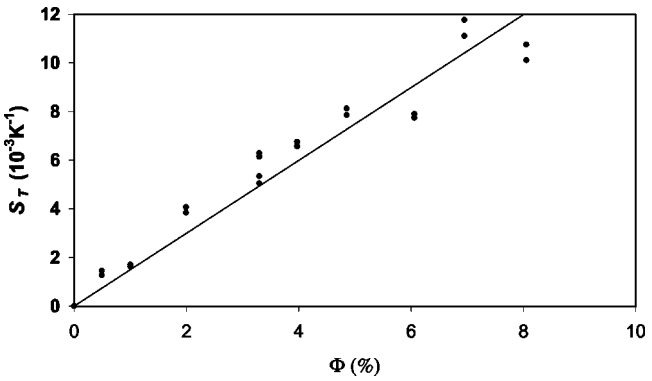

FIG. 8. Proportionality of the Soret coefficient S_T to the volume fraction Φ. Measurements are performed at a fixed pump pulse repetition rate of 1 kHz in a sample of BNE-surfacted maghemite in cyclohexane (CX207BNE, $\Phi=3.3\%$) with a cell thickness of 20 μm and a grating period of 42 μm.

magnetic fluids, at various volume fractions and different temperatures, by means of a total-reflection refractometer. The measured n'_F values are assumed to obey the following linear approximation:

$$n'_F(\Phi,T)=n_S(T_{00})+\alpha\Phi+\beta(T-T_{00}), \tag{7.2}$$

where n_S is the refraction index of the solvent; the best-fit values found for α and β are then identified to $\partial n'_F/\partial\Phi$ and $\partial n'_F/\partial T$, respectively. Values for N^F are given in Table II; some of them are measured with a high precision, others are only estimated.

By studying samples at different dilution rates ($\Phi<8\%$ since at high Φ the Soret effect is meaningless in a ferrofluid as remarked in Sec. III), a second important property of S_T is noticed: S_T is experimentally proved to be proportional to (Fig. 8). This is observed at low Φ and for a given type of colloid, i.e., at fixed nanoparticle size and given particle surrounding, but at different Φ. Therefore the quantity S_T^* defined by

$$S_T^*=S_T(\Phi)/\Phi, \tag{7.3}$$

called here ''reduced Soret coefficient,'' depends only on the type of the colloid. It is a more relevant parameter than S_T for characterizing the Soret effect in a ferrofluid regardless of its dilution rate. In passing, we note that some authors [27–30] call Soret coefficient what is denoted S_T^* in this work. It reflects their expecting that S_T^* could be independent of Φ. The dimensionless quantity X_T^* defined by

$$X_T^*=X^*/(F\tau_{\rm th}\Phi), \tag{7.4}$$

and called here ''reduced concentration contribution,'' is worth considering because (i) it is directly determined from the experimental data X^*, and (ii) it does not depend on Φ as it obeys the following relation [see Eqs. (7.1) and (7.3)]:

$$X_T^*=N^F S_T^*, \tag{7.5}$$

which is used hereafter to determine S_T^* from X_T^*.

A Soret velocity $\mathbf{v}_S$ can be defined by equating the Soret volume-fraction flow $\mathbf{J}_m^S$ [second term of the right-hand side of Eq. (3.1)] to $\Phi\mathbf{v}_S$. Similarly, an algebraic (equivalent) ''Soret mobility'' μ_S can be defined by

$$\mathbf{v}_S=-\mu_S\boldsymbol{\nabla}(k_BT), \tag{7.6}$$

in analogy to the other linear transport phenomena. In the above definition, the Boltzmann constant k_B is used to keep to μ_S the usual mobility unit. The Soret mobility is related to S_T^* through

$$\mu_S=D_mS_T^*/k_B. \tag{7.7}$$

As S_T^* and therefore μ_S, do not depend on Φ, i.e., on the concentration of particles, the Soret effect is proved here not to be a collective phenomenon, but a particle one. As a consequence, the thermodiffusive mechanism has to do with the interaction of each individual particle with its solvent surrounding.

Since in Eq. (3.1) the actual coefficient relating $\mathbf{J}_m^S$ to $\boldsymbol{\nabla}T$ is the product D_mS_T, μ_S is the parameter that characterizes the velocity response to a temperature gradient in the Soret effect. No direct determination of μ_S is given here, but an indirect one consists in determining D_m separately from S_T^* according to the method described earlier [[5,8,13], see also Eq. (4.13)]. The evaluation of the force $\mathbf{F}_S$ causing the Soret effect on a nanoparticle offers another way for studying the Soret effect. According to the Stokes-Einstein relation, $\mathbf{F}_S$ is related to $\mathbf{v}_S$ by

$$\mathbf{F}_S=(k_BT/D_m)\mathbf{v}_S. \tag{7.8}$$

Using Eqs. (7.6) and (7.7), this relation reduces to

$$\mathbf{F}_S=-TS_T^*\boldsymbol{\nabla}(k_BT). \tag{7.9}$$

The dimensionless ratio $\mathbf{F}_S/\boldsymbol{\nabla}(k_BT)=-TS_T^*$ is a relevant parameter for characterizing the response of a nanoparticle to a gradient of temperature in term of a force. To sum up, two complementary descriptions, in velocity and force, of the nanoparticle response, lead to two complementary parameters, μ_S and TS_T^*, for characterizing the Soret effect.

VIII. PARTICLE SURROUNDING (COATING AND SOLVENT)

In order to determine systematically the thermodiffusive properties of different ferrofluids, we have evaluated X, $\tau_{\rm th}$, X^*, X_T^*, S_T^*, and μ_S, successively. The first three quantities are found from experiments on samples at different dilution rates and under different experimental conditions, whereas X_T^* is a best fit or an average value; S_T^* and μ_S are then determined from Eqs. (7.5) and (7.7).

Table I gives the structures of the six ferrofluids we have studied, as well as the nanoparticle core radius R_{RX} and the hydrodynamic one R_H. R_H is found to be larger than R_{RX}, which is expected because of the thickness of the nanoparticle coating. Table II gives (i) elements for evaluating the calibration factor N^F, and (ii) thermodiffusive parameters

that do not depend on the dilution rate: X_T^*, S_T^*, and μ_S. Table II calls for the following comments (some of them have been already presented above):

The calibration factor N^F is about five times larger in ionic ferrofluids than in surfacted ones because $\partial n'_F/\partial T$ is much weaker in water than in organic solvents.

A first comparison between magnetic colloids shows that (i) as previously observed, S_T^* is positive in surfacted samples and negative in ionic ones, (ii) $|S_T^*|$ varies by more than a factor of 15, but there seems to be no strong difference in $|S_T^*|$ between ionic ferrofluids and surfacted ones (the statistics from six samples is poor, however), and (iii) as the experimental volume-fraction contribution X in Eq. (5.13) is more unstable in ionic ferrofluids than in surfacted ones, Soret parameters are less accurately determined in ionic ferrofluids than in surfacted ones.

Among the three studied surfacted colloids, the two samples sharing the same surfactant (BNE), but dispersed in different solvents, give almost the same value for S_T^*.

We have shown above that the thermodiffusive mechanism is located in each particle and its solvent surrounding. Analyzing S_T^* and μ_S data in Table II provides more precise hints to the origin of the force driving the particles of a magnetic colloid under a temperature gradient: the value of S_T^*, and even its sign, can change from a ferrofluid to another while keeping the same core, which proves that the Soret properties depend little on the particle-core nature and very much on the particle surrounding (coating and nearby solvent). The thermodiffusion mechanism has to be searched in the particle-surrounding region, and this is contemplated for future work. Therefore, thermodiffusive properties of ferrofluids seem not to be directly connected to the magnetic ones whose origin is localized in the nanoparticle cores.

IX. CONCLUSION

In our previous FRS works on magnetic colloids, it was mentioned that dielectrophoresis might not be the only origin of the nanoparticle drift in a pump-laser-beam interference pattern, and that a thermodiffusive effect could also be put forward. While dielectrophoresis is directly due to the space modulation of the incident electromagnetic field, the second effect is more complex: the light-intensity modulation generates, by absorption, a temperature modulation, which, in turn, induces a particle flow and therefore a particle-concentration modulation. These two modulations provide additional contributions to the diffracted electromagnetic field. This paper has shown how to distinguish them. They follow different time evolutions and, as temperature is a faster variable than concentration, the time characteristics of the incident pumping light is chosen so that the concentration contribution to the diffracted field should be observed as a constant background, whereas the temperature modulation would provide a time-periodic contribution whose amplitude could be easily measured. In this method, the temperature modulation serves the dual purpose of generating the concentration modulation and calibrating it in order to eventually determine the value of the Soret coefficient. In other words, a relative photometry technique is proposed whose results are independent of the large uncertainties that beset absolute photometry measurements. For a precise calibration, a model in which the sample temperature and particle concentration are determined simultaneously, has been put forth taking into account thermodiffusion and dielectrophoresis effects. A two-time-scale analysis has been developed that takes advantage of the difference of magnitude in response times of temperature and of particle concentration. A specific solution has been obtained in a two-dimensional approximation when optical pumping is time periodic, giving a powerful method for determining the dielectrophoretic effect and the algebraic value of the Soret coefficient [24,31].

With this tool, many new and sometimes unexpected physical results have been obtained about magnetic colloids [24,31]. First, dielectrophoresis has been shown to be negligible compared to the thermodiffusive effect. Second, the Soret coefficient has been found to be proportional to the particle volume fraction, so that the particle drift velocity is independent of the concentration of nanoparticles. As a consequence, the microscopic origin of the thermodiffusive effect lies in the interplay of the particle and its surrounding; this is embodied in the notion of a one-particle thermodiffusive mobility defined as the ratio of the drift velocity to the gradient of k_BT, or in the ratio of the Soret force to the gradient of k_BT. Third, the thermodiffusive mobility is found to be positive in all ionic ferrofluids, in contrast to that measured in surfacted ones. An investigation of the thermodiffusive mechanism is planned for future work.

ACKNOWLEDGMENTS

We want to thank E. Bringuier for fruitful remarks. We are very thankful to V. Cabuil, S. Neveux, A. Bée, and D. Talbot for providing us so kindly with all the different magnetic fluids we wanted together with precious information about them. We do not forget B. M. Heegaard, A. Mezulis, F. da Cruz, C. Mouchet, H. Avansi, and H. Sebbah, whose measurements lent more accuracy to our N^F and X values. We also thank A. Cebers, R. Perzynski, and E. Blums for very fruitful discussions.

APPENDIX: DIFFRACTION BY A MIXED TEMPERATURE AND CONCENTRATION GRATING

In this section, for the sake of simplicity, the formulas will exhibit no explicit time dependence, as they should do. The space-periodic modulations of the particle volume fraction and of the temperature generate absorption and index gratings in the sample. They are studied by measuring the diffracted intensity I_d of a probe laser beam. Under normal incidence, the electric field diffracted in the ψ direction has the following dependence:

$$E_d(\psi) \propto \int_{-x_0}^{x_0} \exp\left[\frac{2\pi i}{\lambda_t}\left(n_0 x \sin\psi + \int_{-e}^{l+e} \tilde{n}(x,z)\,dz\right)\right] dx\,, \tag{A1}$$

in which λ_t, x_0, and n_0 are the probe wavelength, the beam half-width, and the index of refraction at λ_t outside the sample, respectively. The sample being made up of two glass plates surrounding a magnetic colloid layer, $\tilde{n}(x,z)$ stands for both materials at λ_t in Eq. (A1). For $0<z<l$, $\tilde{n}$ is the complex refraction index $\tilde{n}_F$ of the magnetic colloid, whereas for $-e<z<0$ and $l<z<l+e$, $\tilde{n}$ is the real refraction index n_G of the glass. Actually $\tilde{n}$ is a function of T and, in the colloid layer, of Φ; they are themselves functions of x, z, and t. In a linear approximation and without any vibration or convection effect, the complex refraction index in the colloid can be expanded as [see Eqs. (4.4) and (4.5)]

$$\tilde{n}_F=\tilde{n}_F(T_{00},\Phi_{00})+\frac{\partial\tilde{n}_F}{\partial T}[T_0(z)-T_{00}]+\frac{\partial\tilde{n}_F}{\partial\Phi}[\Phi_0(z)-\Phi_{00}]+\left[\frac{\partial\tilde{n}_F}{\partial T}T_1(z)+\frac{\partial\tilde{n}_F}{\partial\Phi}\Phi_1(z)\right]\cos qx, \tag{A2}$$

where T_{00} is a mean temperature whose precise definition is immaterial in a linear formulation. A similar expression can be given for n_G that is a real function of T alone. Upon expanding the exponential function in Eq. (A1) in Bessel functions J_k, and using relation (A2), the intensity I_d^k diffracted at order k obeys the following proportionality relation:

$$I_d^k\propto|J_k((\tilde{L}_{F1}+L_{G1})2\pi/\lambda_t)|^2, \tag{A3}$$

where the proportionality coefficient does not depend on k, and $\tilde{L}_{F1}$ and L_{G1} are, respectively, the first-order Fourier components of the optical paths in the colloid and in the glass plate with respect to x. The first one is expressed as [see Eqs. (A2), (5.1), and (5.2)]

$$\tilde{L}_{F1}=l\left(\frac{\partial\tilde{n}_F}{\partial T}T_{F1}+\frac{\partial\tilde{n}_F}{\partial\Phi}\Phi_{F1}\right). \tag{A4}$$

Similarly, the optical path in the glass plate can be expressed as [see Eq. (5.3)]

$$L_{G1}=l\frac{\partial n_G}{\partial T}T_{G1}. \tag{A5}$$

In Eq. (A3), the complex argument $(\tilde{L}_{F1}+L_{G1})2\pi/\lambda_t$ of the function J_k is assumed to have a modulus much lower than unity; this is *a posteriori* justified by the numerical values found in Sec. VIII. The following approximate formula gives then the ratio of the first-order-diffracted intensity to the transmitted one:

$$I_d^{k=1}/I_d^{k=0}=(2\pi/\lambda_t)^2|\tilde{L}_{F1}+L_{G1}|^2. \tag{A6}$$

Absorption effects have no action on this ratio, as they reduce both intensities by the same factor. The ratio is related to the modulations of Φ and T in both media by the following expansion:

$$I_d^{k=1}/I_d^{k=0}=(2\pi l/\lambda_t)^2\times(A_FT_{F1}^2+B_F\Phi_{F1}^2+C_FT_{F1}\Phi_{F1}+A_GT_{G1}^2+C_{FG}T_{G1}\Phi_{F1}+D_{FG}T_{F1}T_{G1}), \tag{A7}$$

where the parameters A_F, B_F, C_F, A_G, C_{FG}, and D_{FG} are defined by:

$$A_F=\left(\frac{\partial n_F'}{\partial T}\right)^2+\left(\frac{\partial n_F''}{\partial T}\right)^2,\quad B_F=\left(\frac{\partial n_F'}{\partial\Phi}\right)^2+\left(\frac{\partial n_F''}{\partial\Phi}\right)^2,$$

$$C_F=2\left(\frac{\partial n_F'}{\partial T}\frac{\partial n_F'}{\partial\Phi}+\frac{\partial n_F''}{\partial T}\frac{\partial n_F''}{\partial\Phi}\right),$$

$$A_G=\left(\frac{\partial n_G}{\partial T}\right)^2,\quad C_{FG}=2\frac{\partial n_F'}{\partial\Phi}\frac{\partial n_G}{\partial T},\quad D_{FG}=2\frac{\partial n_F'}{\partial T}\frac{\partial n_G}{\partial T}, \tag{A8}$$

and n_F' and n_F'' are the real and imaginary parts of the complex refraction index of the colloid. In Eqs. (A6) and (A7) it is assumed that $I_d^{k=0}$ is independent of the modulations of T and Φ.

[1] E. Guyon, P. Jenffer, A. d'Arco, and M. Cloitre, Eur. J. Phys. **2**, 193 (1981).

[2] R. I. Scarlet, Phys. Rev. A **6**, 2281 (1972).

[3] D. W. Pohl, S. E. Schwartz, and V. Irniger, Phys. Rev. Lett. **31**, 32 (1973).

[4] H. Eichler, G. Saljje, and H. Stahl, J. Appl. Phys. **44**, 5383 (1973).

[5] J.-C. Bacri, A. Cebers, A. Bourdon, G. Demouchy, B. M. Heegaard, and R. Perzynski, Phys. Rev. Lett. **74**, 5032 (1995).

[6] R. E. Rosensweig, *Ferrohydronamics* (Cambridge University Press, Cambridge, England, 1985).

[7] *Magnetic Fluids and Applications—Handbook*, edited by B. Berkovsky and M. Khartov (Begell House, New York, 1994).

[8] J.-C. Bacri, A. Cebers, A. Bourdon, G. Demouchy, B. M. Heegaard, B. Katshevsky, and R. Perzynski, Phys. Rev. E **52**, 3936 (1995).

[9] V. Cabuil, S. Neveu, and R. E. Rosensweig, J. Magn. Magn. Mater. **122**, 437 (1993).

[10] D. P. Jackson, R. E. Golstein, and A. Cebers, Phys. Rev. E **50**, 298 (1994).

[11] J.-C. Bacri, A. Cebers, and R. Perzynski, Phys. Rev. Lett. **72**, 2705 (1994).

[12] J.-C. Bacri, A. Cebers, J.-C. Dabadie, and R. Perzynski, Europhys. Lett. **27**, 437 (1994).

[13] G. Demouchy, A. Bourdon, J.-C. Bacri, F. da Cruz, A. Mezulis, and E. Blums, in *Proceedings of the 4th International PAMIR Conference on Magnetohydrodynamics at Dawn of Third Millennium*, edited by A. Alemany (LEGI, Grenoble, 2000), p. 433.

[14] E. Blums, S. Odenbach, A. Mezulis, and M. M. Maiorov, Phys. Fluids **10**, 2155 (1998).

[15] P. Fabre, C. Casagrande, M. Veyssié, V. Cabuil, and R. Mas-

sart, Phys. Rev. Lett. **64**, 539 (1990).
[16] J.-C. Bacri and A. M. Figueiredo Neto, Phys. Rev. E **50**, 3860 (1994).
[17] J. Bibette, J. Magn. Magn. Mater. **122**, 37 (1993).
[18] B. Jean-Jean, E. Freysz, A. Poton, A. Ducasse, and B. Pouligny, Phys. Rev. A **39**, 5268 (1989).
[19] E. Freysz, E. Laffon, J. P. Delville, and A. Ducasse, Phys. Rev. E **49**, 2141 (1994).
[20] S. R. de Groot, *L'effet Soret* (N.V. Noord-Hollandsche Uitgevers Maatschappij, Amsterdam, 1945).
[21] R. Massart, IEEE Trans. Magn. **17**, 1247 (1981).
[22] L. Landau and E. Lifchitz, *Fluid Mechanics* (Pergamon Press, Oxford, 1959).
[23] A. Sommerfeld, *Electrodynamik* (Akademische Verlagsgesellschaft Geest und Portig KG, Leipzig, 1949).
[24] J. Lenglet, Ph.D. thesis, Université Paris 7–Denis Diderot, Paris, 1996, p. 144.
[25] *Handbook of Chemistry and Physics*, 76th ed., edited by D. R. Lide (CRC Press, Boca Raton, 1995), pp. 6–254.
[26] A. Mezulis, E. Blums, A. Bourdon, and G. Demouchy, in *Proceedings of the 4th International PAMIR Conference on Magnetohydrodynamics at Dawn of Third Millennium* (Ref. [13]), p. 781.
[27] A. Mezulis, Ph.D. thesis, Université Paris 7–Denis Diderot, Paris, 1999.
[28] T. Völker, E. Blums, and S. Odenbach, in *Proceedings of the 4th International Meeting on Thermodiffusion, Bayreuth, Germany*, edited by W. Köhler and S. Wiegand (Universität Bayreuth Press, Bayreuth, 2000), p. 38.
[29] G. Labrosse, in *Proceedings of the 4th International Meeting on Thermodiffusion, Bayreuth, Germany* (Ref. [28]), p. 30.
[30] K. I. Morozov, in *Proceedings of the 4th International Meeting on Thermodiffusion, Bayreuth, Germany* (Ref. [28]), p. 59.
[31] A. Bourdon, G. Demouchy, J. C. Bacri, and E. Blums, in *Proceedings of the 4th International Meeting on Thermodiffusion, Bayreuth, Germany* (Ref. [28]), p. 48.
[32] R. Massart, E. Dubois, V. Cabuil, and E. Hasmonay, J. Magn. Magn. Mater. **149**, 1 (1995).